

Converting Brownmillerite to Alternate Layers of Oxygen-Deficient and Conductive Nano-Sheets with Enhanced Thermoelectric Properties

Songbai Hu, Wenqiao Han, Xiaowen Li, Mao Ye, Yao Lu, Cai Jin, Qi Liu, Junling Wang, Jiaqing He, Claudio Cazorla, Yuanmin Zhu,* and Lang Chen*

Introducing large oxygen deficiencies while retaining low resistivity is important for enhancing the overall thermoelectric properties in 3d transition-metal oxides. In this study, a new synthesis route to reconstruct the insulating brownmillerite $\text{SrCoO}_{2.5}$ is adapted. Through a step-by-step nano-blocks modification, a series of highly-conductive layered structures is evolved, which are $[\text{Sr}_2\text{O}_2\text{H}_2]_{0.5}\text{CoO}_2$, $[\text{Sr}_2\text{O}_2]_{0.4}\text{CoO}_2$, and $[\text{Sr}_2\text{CoO}_3]_{0.57}\text{CoO}_2$, while still retaining considerable Seebeck coefficient ($\approx 100 \mu\text{V K}^{-1}$). Coexistence of low resistivity and high oxygen deficiency is realized in the latter two polymorphs by forming a majority of sintered oxygen vacancies in the rock-salt layer and a minority of normal oxygen vacancies in the CoO_2 layer. A room-temperature in-plane power factor of $3.6 \text{ mW K}^{-2} \text{ m}^{-1}$, power output density of 4.5 W m^{-2} at a temperature difference of 28 K, and an out-of-plane thermal conductivity of $0.33 \text{ W K}^{-1} \text{ m}^{-1}$ are obtained in the $[\text{Sr}_2\text{O}_2]_{0.4}\text{CoO}_2$ thin film that exhibits the highest oxygen deficiency ($\delta = 2.95$), which is on par with Bi_2Te_3 , the benchmark. It is pointed out that proper distribution of oxygen vacancy is essential in tailoring the physical and chemical properties of transition-metal oxides. The sintered/normal oxygen vacancy layer model provides guidance to the exploration of materials with both low electric resistivity and thermal conductivity.

green-energy technological applications and devices like electrochemical catalysis, fuel cells, and thermoelectric electrodes. Stabilized $\text{V}_\text{O}^\bullet$ have been considered to be highly efficient for oxygen evolution reaction.^[5,6] In oxide fuel cells, the ionic diffusion in electrodes must be occurring via migration of oxide ions jumping into an adjacent vacant site.^[7] Defects like oxygen vacancies typically act as efficient phonon scattering centers which reduce the phonon mean-free paths and thus deplete the corresponding lattice thermal conductivity.^[8,9] On the other hand, the introduction of $\text{V}_\text{O}^\bullet$ into a crystal ($\text{O}_\text{O}^\times + 2\text{h}\bullet \rightarrow \text{V}_\text{O}^\bullet + 1/2\text{O}_2$, where O_O^\times and $\text{h}\bullet$ represent oxygen at lattice site and hole, respectively) would naturally consume the carriers, thereby decrease the electronic conductivity. Examples like in $\text{ABO}_{3-\delta}$ ($\text{A} = \text{Ca, Sr, La}$; $\text{B} = \text{Cr, Mn, Fe, Co, Ni}$) the switch from high to low oxygen content structure usually yields highly suppressed electronic conduction,^[10-17]

1. Introduction

Oxygen vacancies ($\text{V}_\text{O}^\bullet$) and oxygen deficiency (δ) play a key role in tailoring the functional properties of 3d transition-metal oxides, like defect-induced ferromagnetism^[1,2] insulator-to-metal transitions,^[3,4] and affecting their applicability to

which trades off the advantages brought by $\text{V}_\text{O}^\bullet$. Therefore, coexisting low electronic resistivity and large oxygen deficiency remains a big challenge. A general methods in dealing with this issue was to substitute A/B-site with acceptor cations that exhibit lower valence states, thereby creates oxygen deficient materials,^[7] or import microstructures that separate conductive domains from $\text{V}_\text{O}^\bullet$ enrichment regions like those in polycrystalline ceramics.^[18] However, carriers would be inevitably scattered by oxygen vacancies or domain boundaries and result in a reduced mobility. While in this work, we introduced a different strategy, that is, to form isolated oxygen deficient nano-sheet from the conductive layer at the atomic level, to address this concern. We exemplified this strategy by converting the insulating brownmillerite $\text{SrCoO}_{2.5}$ (BM-SCO) to alternating layers of oxygen-deficient and conductive nano-sheets. The $\text{V}_\text{O}^\bullet$ structurally locked in rock salt (RS) insulating layer did not interfere the electronic conduction of the other layer and significantly suppressed the thermal conductivity. Meanwhile, the converted structure retained considerable Seebeck coefficient as its parent even though the conductivity was highly improved, thus obtained enhanced thermoelectric properties.

BM-SCO is orthorhombic with lattice constants $a = 5.5739 \text{ \AA}$, $b = 5.4697 \text{ \AA}$, and $c = 15.7450 \text{ \AA}$, which can be viewed as

S. Hu, W. Han, X. Li, M. Ye, Y. Lu, C. Jin, Q. Liu, J. Wang, J. He, L. Chen
Department of Physics
Southern University of Science and Technology
Shenzhen 518055, China
E-mail: chenlang@sustech.edu.cn

C. Cazorla
Departament de Física
Universitat Politècnica de Catalunya
Campus Nord B4-B5, Barcelona E-08034, Spain

Y. Zhu
School of Material Science and Engineering
Dongguan University of Technology
Dongguan 523000, China
E-mail: zhuyuanm@dgut.edu.cn

 The ORCID identification number(s) for the author(s) of this article can be found under <https://doi.org/10.1002/aenm.202201469>.

DOI: 10.1002/aenm.202201469

pseudo-tetragonal ($a_t = 3.905$ and $c_t = 7872$ Å).^[19] It is consisted by alternatively stacked Co–O octahedra and tetrahedra along the (001) direction, and characterized by columns of ordered V_{O}^{\bullet} along its pseudo-tetragonal [110] direction. Although BM-SCO exhibits considerable Seebeck coefficient ($\approx 100 \mu\text{V K}^{-1}$)^[20] and thermal conductivity ($\approx 1.5 \text{ W K}^{-1} \text{ m}^{-1}$),^[21] it is very insulating at room and low temperature ($>10^3 \text{ m}\Omega \text{ cm}$) as a result of high oxygen deficiency,^[12] thereby demonstrates a really poor thermoelectric properties. BM-SCO thin film could be oxidized to perovskite $\text{SrCoO}_{3-\delta}$ ($0 \leq \delta < 0.25$),^[19] reduced to square tube SrCoO_2 ,^[13] or form $\text{H}_x\text{SrCoO}_{2.5}$ phase by intercalation of hydrogen.^[22,23] However, attempts in achieving both low resistivity and high oxygen deficiency structures have yet been successful.

2. Results and Discussion

Figure 1 shows the preparation of three Sr–Co–O (SCO) thin films from BM-SCO thin film grown on (001) (La,Sr)(Al,Ta)O₃ (LSAT) substrates and the XRD characterization on the newly synthesized SCO10, SCO9, and SCO8 thin films (named by their lowest diffraction angles which are $\approx 10^\circ$, 9° , and 8° , respectively).

The thickness of BM-SCO film was estimated to be 70 nm in approximate from X-ray reflectivity measurement. As shown in Figure 1a, BM-SCO evolved to three SCOs by experiencing a step-by-step phase transformation. Figure 1b demonstrates XRD θ – 2θ scans of the four SCO thin films. The trend that 2θ shifts to the lower angle indicates a decreasing and tunable periodicity in SCO thin films by temperature control. Correspondingly, the c -lattice constant increases from 9.02 to 9.77 Å, and then to 11.06 Å step-by-step from SCO10, SCO9 to SCO8. Figure 1c illustrates the in situ phase transformation with temperature dependent XRD by heating the sample in wet air (relative humidity $\approx 79\%$). At 250 °C BM-SCO started to transform to SCO10. At 480 °C, SCO10 began to transform to SCO9. By further annealing the thin film at 580 °C, the SCO10 disappeared and SCO8 began to form. Although mixed phases were observed during the fast-heating process, single phases could be obtained by annealing the sample for longer time, see Experimental Section.

The in-plane crystallographic geometry of SCO10, SCO9, and SCO8 were determined by wide area reciprocal space mapping in Figure 1d–f. It is found that two different crystallographic geometries, that is, triclinic (T) and hexagonal (H) layers and their 90° rotation counterpart, coexist in each thin

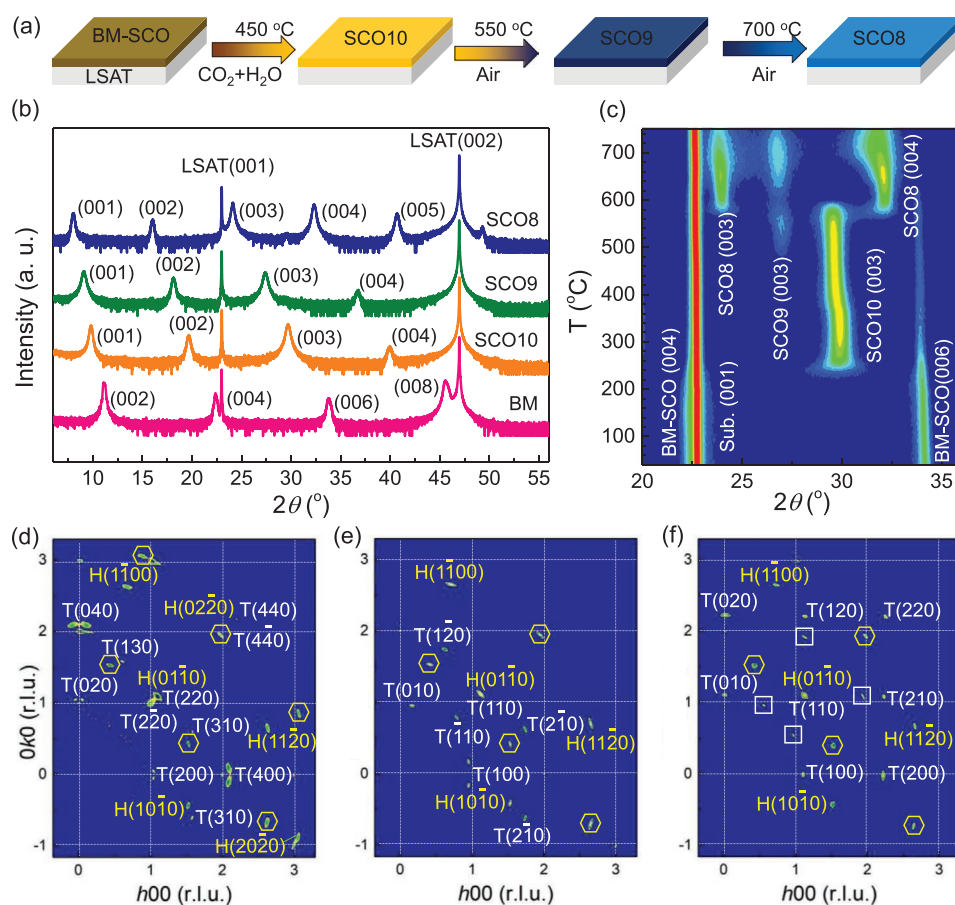


Figure 1. a) Schematic preparation of SCO10, SCO9, and SCO8 from BM-SCO thin film. b) XRD θ – 2θ scans of as-prepared BM-SCO, SCO10, SCO9, and SCO8 thin films grown on LSAT substrates. c) In situ XRD peak evolution of BM-SCO thin film as heating in wet air. d–f) The in-plane wide area reciprocal space mapping for SCO10, SCO9, and SCO8 thin films, respectively. The q coordinates have been divided by LSAT q_{100} . The white grids corresponding to the integers h, k are guides to eyes. The T and H in the crystal plane index represent the triclinic rock salt layer [SrO]/[SrCoO] and the hexagonal CoO₂ layer, respectively. The spots of rotated CoO₂ layer are marked by yellow hexagons, while the rotated SrCoO layer is marked by white squares.

Table 1. Structure and composition parameters of layered SCO thin films.

	Layer	$a[\text{\AA}]$	$b[\text{\AA}]$	$c[\text{\AA}]$	$\alpha/\gamma[^\circ]$	$\beta[^\circ]$	q	Formula	V(Co)nominal	V(Co)actual	δ
SCO10	Sr ₂ O ₂ H ₂	2.518	2.804	9.02	90	95.5	0.5	SrCoO _{3-δ} H	3+	2.84+	0.08
	CoO ₂	2.518	2.802								
SCO9	Sr ₂ O ₂	2.449	3.470	9.76	90	96	0.4	Sr ₄ Co ₅ O _{14-δ}	4+	2.82+	2.95
	CoO ₂	2.449	2.816								
SCO8	Sr ₂ CoO ₃	2.469	2.469	11.06	90	94.3	0.57	Sr ₃ Co ₄ O _{9.76-δ}	3.38+	2.96+	0.84
	CoO ₂	2.469	2.808								

film, which correspond to the RS layer and the CdI₂-type CoO₂ layer according to the below scanning transmission electron microscopy (STEM) analysis, respectively. The fourfold geometry of RS layer and sixfold geometry of CoO₂ layer are confirmed by the in-plane phi-scans in Figure S1, Supporting Information. These two geometries can be orthogonalized in in-plane directions by their diagonals, and the diagonalized lattice parameters a ($=d_{\text{RS}(110)} = d_{\text{CoO}_2(01\bar{1}0)}$) and b ($=d_{\text{RS}(1\bar{1}0)} = 2d_{\text{CoO}_2(2\bar{1}\bar{3}0)}$) are directly calculated from the in-plane θ - 2θ scans in Figure S2, Supporting Information. The epitaxial relationship between the SCO thin films and the LSAT substrate are RS [110] \parallel CoO₂ [01 $\bar{1}$ 0] \parallel LSAT [110] and RS [1 $\bar{1}$ 0] \parallel CoO₂ [2 $\bar{1}$ 30] \parallel LSAT [1 $\bar{1}$ 0], see Figure S3, Supporting Information. The lattice parameters are summarized in **Table 1**. Regarding the in-plane directions, the a and b lattice parameters of the CoO₂ layers change only slightly for SCO10, SCO9, and SCO8, implying that the hexagonal lattice frame of the SCO thin films is quite stable upon thermal annealing. However, the lattice parameters of the RS layers greatly vary among the different polymorphs, thus providing large tunability via modification of the integrated RS nano-sheets.

High resolution STEM (HR-STEM) was carried out to determine the atomic structure of these SCO thin films. **Figure 2** displays the high-angle annular dark field (HADDF)-STEM, energy dispersive X-ray spectroscopy (EDS) mapping and annular bright field (ABF) images for SCO10, SCO9, and SCO8. **Figure 2a,b** shows the (110) and (100) atomic planes of SCO10, respectively. Similar to that treated in O₂ + H₂O,^[24] the SCO10 is identified as alternatively stacked rock-salt type Sr₂O₂H₂ and CdI₂-type CoO₂ layers. **Figure 2c,d** shows the (110) and (1 $\bar{1}$ 0) atomic planes of SCO9, respectively. We imaged the (1 $\bar{1}$ 0) rather than the (100) plane by considering that the (100) plane rotates too much ($\approx 10^\circ$, see **Figure 1d**) from the LSAT (100). Compared to SCO10, a dark strip within the Sr₂O₂ layer is observed in the HADDF image after H₂O dissolution. The ABF image shows that oxygen atoms in Sr₂O₂ layer of SCO9 take much more spacing along [001] direction than that in SCO10 between the neighboring Sr layers, which is responsible for the increase in c -lattice constant. Meanwhile, the Sr–Sr distance along the b -axis increases dramatically from 2.804 Å in SCO10 to 3.47 Å in SCO9. Such a lattice expansion indicates that there may be a considerable number of V_O^{••} in SCO9. **Figure 2e,f** shows the (110) and (100) atomic planes of SCO8, respectively. In comparison to SCO10 and SCO9, an additional Co–O layer is captured within the Sr₂O₂ layer. The corresponding EDS mapping shows that the Co atom occupies the body center of Sr cube. The ABF images show that the oxygen arrangement in SCO8 follows the rock-salt stacking manner as well. Thus, this layer is identified

to be Sr₂CoO₃, while the CoO₂ layer remains unchanged. The β angle between a and c in these layered-SCOs is determined by the fast Fourier transformation of the (110) atomic plane in **Figure S4**, Supporting Information. The atomic structure of the three layered-SCOs are built up based on the XRD and HR-STEM, and are shown in **Figure 5b–d**.

The structure and composition parameters of these layered SCOs are summarized in **Table 1**. Their formulas can be written as [Sr₂O₂H₂]_{0.5}CoO₂ (SrCoO₃H), [Sr₂O₂]_{0.4}CoO₂ (Sr₄Co₅O₁₄), and [Sr₂CoO₃]_{0.57}CoO₂ (Sr₃Co₄O_{9.76}), assuming the absence of V_O^{••} in each sub-layer. The nominal valence state of Co ions [V(Co)] for each of the layered-SCO thin film is determined to be 3+, 4+, and 3.38+, respectively. However, from the preparation point of view, the oxidization from Co³⁺ to Co⁴⁺ ions by only air-annealing was an arduous work.^[19,25] Thus, the formation of Co⁴⁺ in SCO9 is less likely. We exclude the formation of Sr vacancies based on the facts that Sr is non-volatile and that the successive preparation of from SrCoO_{2.5} to SrCoO₃H, Sr₄Co₅O₁₄ and then Sr₃Co₄O_{9.76} guarantees adequate supply of precursor to the subsequent phase transformation. We would also like to highlight the uniqueness of the [Sr₂O₂]_{0.4}CoO₂ structure as its RS layer is electrically zero charged. To date, nearly all reported misfit-layered compounds integrate positively charged RS plate. The SCO9 may produce high concentration of V_O^{••} as the nominal 4+ of Co ions is far from the normal 3+ valence state. As seen above, BM-SCO transforms to a serial of layered-SCOs by experiencing a cations reconstruction, which establishes a new route to synthesis layered oxides with variable integrated nano-blocks.

X-ray absorption spectra (XAS) were collected at the Co L-edge and O K-edge to probe the oxygen deficiency as well as the electronic structures of these SCO thin films. The results are shown in **Figure 3a,b**, respectively. The XAS of BM-SCO is given for comparison. The schematic electronic structures for [Co(III) 3d-O 2p]_O, [Co(II) 3d-O 2p]_T, and [Co(III) 3d-O 2p]_T hybridization are shown in **Figure 3c–e**, respectively. The subscript O or T denotes the octahedra or triangular crystal ligand field. In the octahedra crystal ligand field (BM-SCO), the [Co(III) 3d-O 2p]_O splits into a high energy e_g band and a low energy t_{2g} band.^[26] The transition of the electrons from O 1s to the unoccupied t_{2g} and e_g bands are represented by A and B, respectively. While in the triangular crystal ligand field (layered SCOs), the t_{2g} band splits into a_{1g} and e_g' bands in further.^[27] The transition of electrons from O 1s to the unoccupied a_{1g} and e_g' band are represented by α , β , respectively. In **Figure 3a**, the line shapes of Co L-edge in SCO10, SCO9, and SCO8 are quite similar to the Co₃O₄,^[28] indicating that there coexist Co(III) and Co(II) in layered SCOs. The less pronounced pre-shoulder in

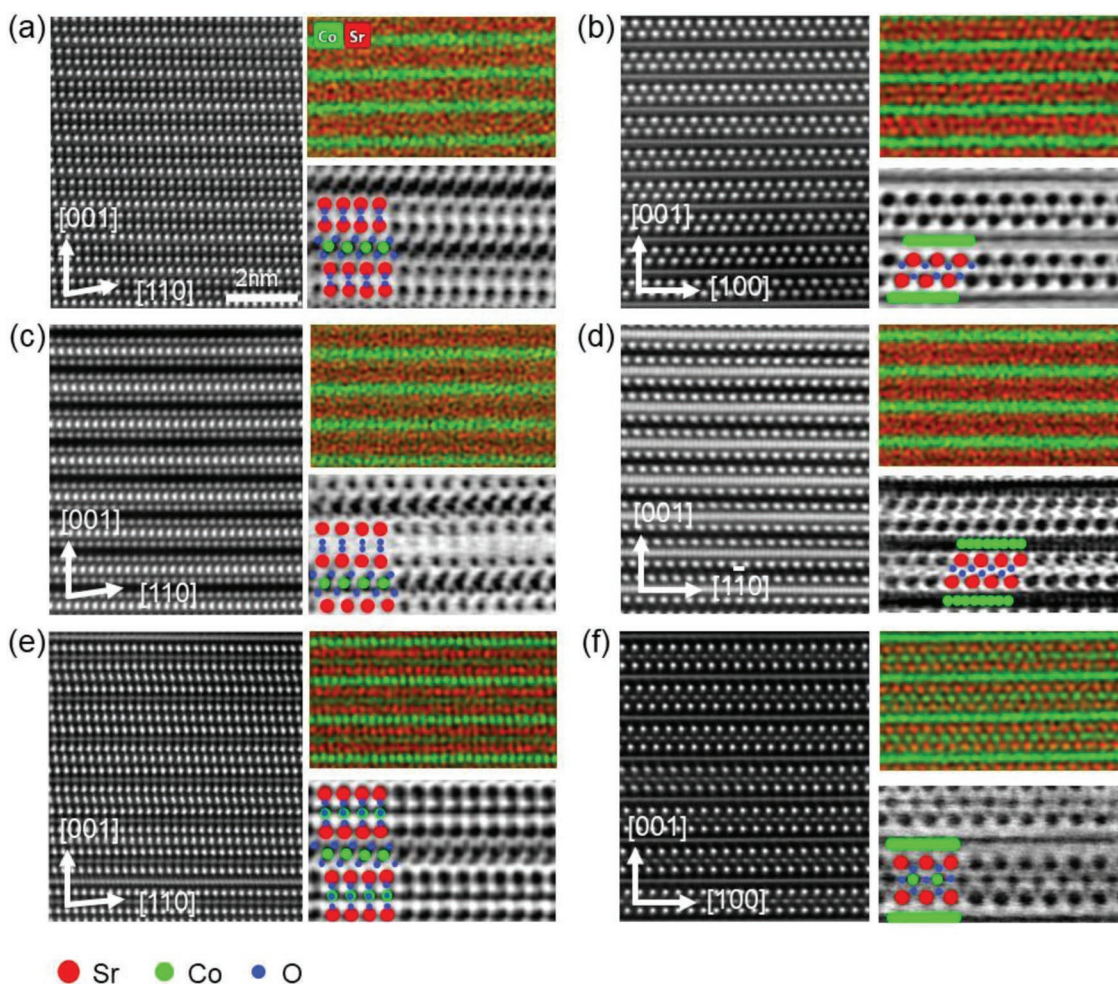


Figure 2. HADDF-STEM, EDS mapping, and ABF images for layered-SCO thin films: a) (110) and b) (100) plane of SCO10; c) (110) and d) ($\bar{1}\bar{1}0$) plane of SCO9; e) (110) and f) (100) plane of SCO8. The Sr, Co, and O atoms are painted by red, green, and blue, respectively.

Co L-edge of SCO8 is due to that a part of Co ions occupy the octahedral sites in RS Sr_2CoO_3 layer, thus decreases the number of Co ions in trigonal coordination; while in SCO10 and SCO9 Co ions coordinate only in trigonal coordination. The L_3 peak position reads 780.2, 779.5, 779.5, and 779.6 eV for BM-SCO, SCO10, SCO9, and SCO8, respectively. That implies the valence state of Co ions in the four SCOs orders as BM-SCO > SCO8 > SCO9 \approx SCO10, which is consistent with the below analysis from O K-edge XAS.

Figure 3b shows the evolution of O K-edge of these SCO thin films. In BM-SCO, the electronic configuration in $[\text{Co}(\text{III}) 3d\text{-O } 2p]_{\text{O}}$ hybridized orbital is depicted by a high spin $e_g^2 t_{2g}^4$ ($S = 5/2$) in Figure 3c.^[26] In case of the SCO10, the small bump at low energy side represents the electron transition from the O 1s to the unoccupied a_{1g} of $[\text{Co}(\text{II}) 3d\text{-O } 2p]_{\text{T}}$ hybridized orbital in triangular crystal ligand field.^[24] Its weak intensity implies that the proportion of Co(II) in SCO10 is fairly small. The strong peak β mixes the contribution from the transition to the e_g of $[\text{Co}(\text{II}) 3d\text{-O } 2p]_{\text{T}}$ and $[\text{Co}(\text{III}) 3d\text{-O } 2p]_{\text{T}}$. Therefore, the electronic configuration of SCO10 is primarily a null spin state $e_g^0 a_{1g}^2 e_g^4$ mixed with a small portion of low spin state $e_g^2 a_{1g}^1 e_g^4$. It is worthy to mention that intermediate spin

of Co^{3+} ($e_g^1 a_{1g}^1 e_g^4$) alone can also generate similar feature α and β . However, in experiment (see Figure S5, Supporting Information) it was found that the bump was well preserved when annealing SCO10 in vacuum, but almost undetectable after annealing in 10 bar oxygen since the Co^{2+} was oxidized to Co^{3+} . Thus, the bump at the low energy side of O K-edge in SCO10 arises from Co^{2+} rather than the intermediate spin Co^{3+} . In that sense, the amount of Co^{2+} can be roughly estimated to 16% using the intensity ratio $\alpha/(\alpha + \beta)$.^[27,29–31] The averaged valence state of Co ions in CoO_2 layer $[V(\text{Co})]$ is determined as 2.84+. The chemical composition of SCO10 is thereby $\text{SrCoO}_{2.92}\text{H}$. Similarly, in SCO9 the content of Co^{2+} is estimated to be $\approx 18\%$, and $V(\text{Co}) = 2.82+$. The formula of SCO9 is written as $\text{Sr}_4\text{Co}_5\text{O}_{11.05}$ accordingly. In SCO8, additional features A and B which have the same peak positions as the BM-SCO were observed as the RS Sr_2CoO_3 layer was sandwiched in between CoO_2 triangular layers except for features α and β . In CoO_2 layer the concentration of Co^{2+} is estimated to be 11%, and the $V(\text{Co}) = 2.96+$, assuming that the Co ions in Sr_2CoO_3 layer are 3+ in approximate as that in BM-SCO. The SCO8 is actually $\text{Sr}_3\text{Co}_4\text{O}_{8.92}$. The $V(\text{Co})$ and oxygen deficiency (δ) for the three SCO thin films are summarized in Table 1. According to XAS,

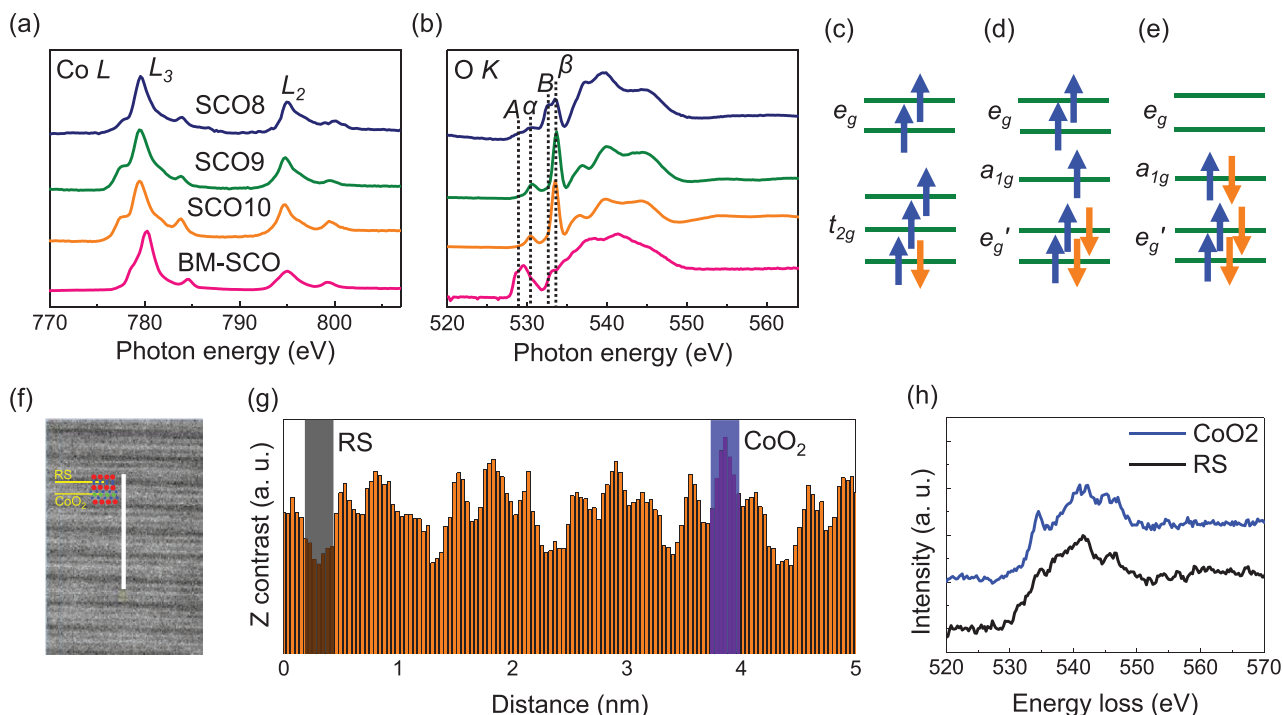


Figure 3. X-ray absorption spectroscopy (XAS) of a) Co *L*-edge, b) O *K*-edge for BM-SCO, SCO10, SCO9, and SCO8 thin films; c–e) the schematic electronic structures for [Co(III) 3d-O 2p]_O, [Co(II) 3d-O 2p]_T, and [Co(III) 3d-O 2p]_T hybridization, respectively; f) TEM image of SCO9 (110) plane; g) Z contrast profile of white line in (f); h) EELS spectra corresponding to the grey- and blue-marked regions in (g).

the oxygen deficiency in layered SCO could be greatly promoted to 0.84 in SCO8 and 2.95 in SCO9 from 0.08 in SCO10, which is mainly attributed to the evolution of RS nano-blocks rather than Co ions as seeing it is quite stable. Figure 3f–h gives the electron energy loss spectroscopy (EELS) for SCO9 which exhibits the highest oxygen deficiency. The grey-marked region in Figure 3g includes the O–O atomic layer within the SrO–OSr RS plate, while the blue-marked area covers the Co–O layer. The EELS for the grey- and blue-marked region in Figure 3g are shown in Figure 3h. The pre-peak near 530 eV arises from the hybridization of O 2p and Co 3d orbitals. It is found that the CoO₂ layer has a higher oxygen content in comparison to that of RS layer as seeing the sharp and strong pre-peak.^[32] Such a finding indicates that a majority of V_O^{••} prefer to stay in RS insulating layer other than CoO₂ conductive layer.

Figure 4 presents the electronic, optical and thermoelectric properties of the BM-SCO, SCO10, SCO9, and SCO8 thin film. In Figure 4a the resistivity (ρ) of SCO10 decreases at least 3 orders of magnitude compared to that of BM-SCO within the temperature range. Interestingly, in higher oxygen deficient SCO8 and SCO9, it decreases another order of magnitude. The SCO9 and SCO8 become even metallic above 50 K. That means high oxygen deficiency does not necessarily suppress electric conduction via proper reconstruction of RS nano-blocks. Figure 4b reveals that the carrier mobility (μ) of SCO9 and SCO8 is significantly enhanced in comparison to that of SCO10. The μ of BM-SCO is not given as it is too insulating. Figure S6, Supporting Information shows that the carrier concentration in these three SCOs is at the level of 10^{21} cm⁻³. Therefore, the increase in conductivity is mainly attributed to

the increase in carrier mobility. Figure 4c shows that in infrared and visible light range SCO10 exhibits the highest transmittance, followed by the SCO8 and then SCO9. In ultraviolet light range the absorption edge of all layered SCOs shift to violet side compared to the BM-SCO. The band gap is estimated to be 2.28, 2.61, 2.75, and 2.79 eV for BM-SCO, SCO10, SCO9, and SCO8, respectively.

According to Figure 4a,b, the response of electric resistivity upon oxygen deficiency in BM-SCO is contrary to the layered-SCOs. In former one high concentration of V_O^{••} usually results in high electronic resistivity;^[4,26] while in latter one it does not harm the electric conduction. The carrier mobility even increases with δ . This fact indicates that a large proportion of V_O^{••} tends to sink in RS insulating layer rather than in CoO₂ conducting layer, or else carriers will be scattered and result in highly suppressed mobility. This finding is consistent with the results shown in Figure 3h. Table 1 shows that the valence of Co ion varies small upon heating in air. Therefore, the content of V_O^{••} in RS layer depends on change of composition or lattice parameters. As these V_O^{••} composed in RS layer are structurally-locked and electrically-isolated, we define them as sintered V_O^{••}. The manipulation of sintered V_O^{••} may lead to the discovery of a layered family. Except for sintered V_O^{••} in RS layer, the decreased carrier mobility and conductivity in SCO10 and SCO8 compared to SCO9 imply a minority of V_O^{••} exists in CoO₂ layer. The formation of SCO9 and SCO8 in air at high temperature actually reduces the number of V_O^{••} in CoO₂ layer. From Figure 4a,b, we estimate that the concentration of minority V_O^{••} in CoO₂ layer orders as SCO9 < SCO8 < SCO10 \leq 0.08. According to Table 1, the total oxygen deficiency is 0.08, 0.84, and 2.95, or

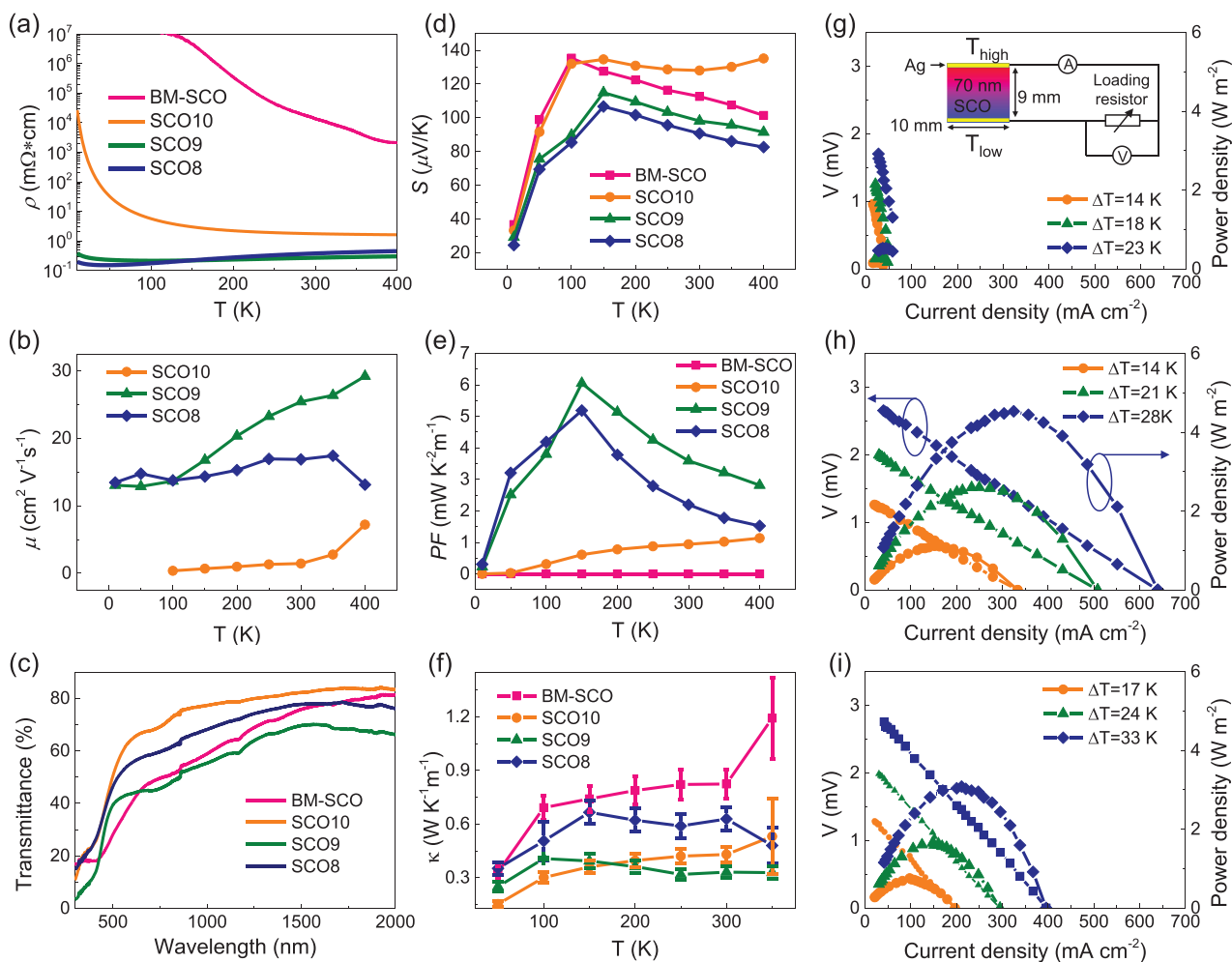


Figure 4. Temperature dependent a) resistivity (ρ), b) carrier mobility (μ), c) optical transmittance, d) Seebeck coefficient (S), e) power factor (PF), and f) thermal conductivity (κ) of BM-SCO and layered-SCO thin films. g–i) The current density versus voltage and power density for SCO10, SCO9, and SCO8 thin films at different ΔT near room temperature, respectively. The inset in (g) illustrates the schematic experiment setup for power output measurement.

0.08/Co, 0.21/Co, and 0.59/Co for SCO10, SCO8, and SCO9, respectively. We refer to Co rather than Sr by considering that the lattice of CoO_2 layer changes slightly among these layered structures. Therefore, the concentration of majority $\text{V}_\text{O}^\bullet$ in RS layer spans 0–0.08, 0.13–0.21, and 0.51–0.59 per Co for each of them. In other words, the content of $\text{V}_\text{O}^\bullet$ in RS layer evolves as $\text{SCO10} < \text{SCO8} < \text{SCO9}$.

Figure 4d shows the experimental Seebeck coefficient (S) of BM-SCO and layered-SCOs over the temperature interval 400–10 K. The positive sign of S implies that both BM-SCO and layered-SCOs are p-type conductors. Although the conductivity of SCO10 improves 3 orders of magnitude as compared to that of BM-SCO, its S is still larger than that of BM-SCO. As a result, the negligible power factor ($\text{PF}, = S^2/\rho$) in BM-SCO is enhanced to $0.9 \text{ mW K}^{-2} \text{ m}^{-1}$ in SCO10 at 300 K (Figure 4e) in in-plane direction. By reconstructing the RS nano-blocks, the PF of SCO9 and SCO8 further amount to 3.6 and $2.2 \text{ mW K}^{-2} \text{ m}^{-1}$ at 300 K, which are $\approx 4 \times 10^4$ and 2.4×10^4 times of that in BM-SCO, respectively. Such performances are

superior to that of sputtered/ceramic $\text{Sr}_3\text{Co}_4\text{O}_9$,^[33,34] or typical transition-metal thermoelectric oxides such as $(\text{Ca}_{0.9}\text{M}_{0.1})\text{MnO}_3$,^[35] SrTiO_3 ,^[36] $\text{Ca}_3\text{Co}_4\text{O}_9$,^[37] and ZnO ,^[38] and comparable to $\text{Na}_x\text{Co}_2\text{O}_4$ which demonstrates the highest room temperature PF ($5 \text{ mW K}^{-2} \text{ m}^{-1}$) and Bi_2Te_3 ($4 \text{ mW K}^{-2} \text{ m}^{-1}$),^[39] see Table S1, Supporting Information. Figure 4g–i) measures the output power density for the three layered-SCO thin films. It can be seen that at similar temperature differences (ΔT) SCO9 thin film exhibits the highest output power density, followed by SCO8 and SCO10. This trend is consistent with the power factor shown in Figure 4e. At $\Delta T = 14, 21$, and 28 K , the power density for SCO9 reads 1.1, 2.6, and 4.5 W m^{-2} , respectively. The normalized power density is thereby calculated between 0.56 and $0.59 \mu\text{W K}^{-2} \text{ cm}^{-2}$, which ranks the top level among those reported Bi_2Te_3 and Bi_2Te_3 -based film devices,^[40–43] see Figure S7, Supporting Information.

Figure 4f shows that the out-of-plane thermal conductivity (κ) of the four SCOs order in $\text{SCO9} < \text{SCO10} < \text{SCO8} < \text{BM-SCO}$ above 150 K. The κ was obtained by using a time-domain

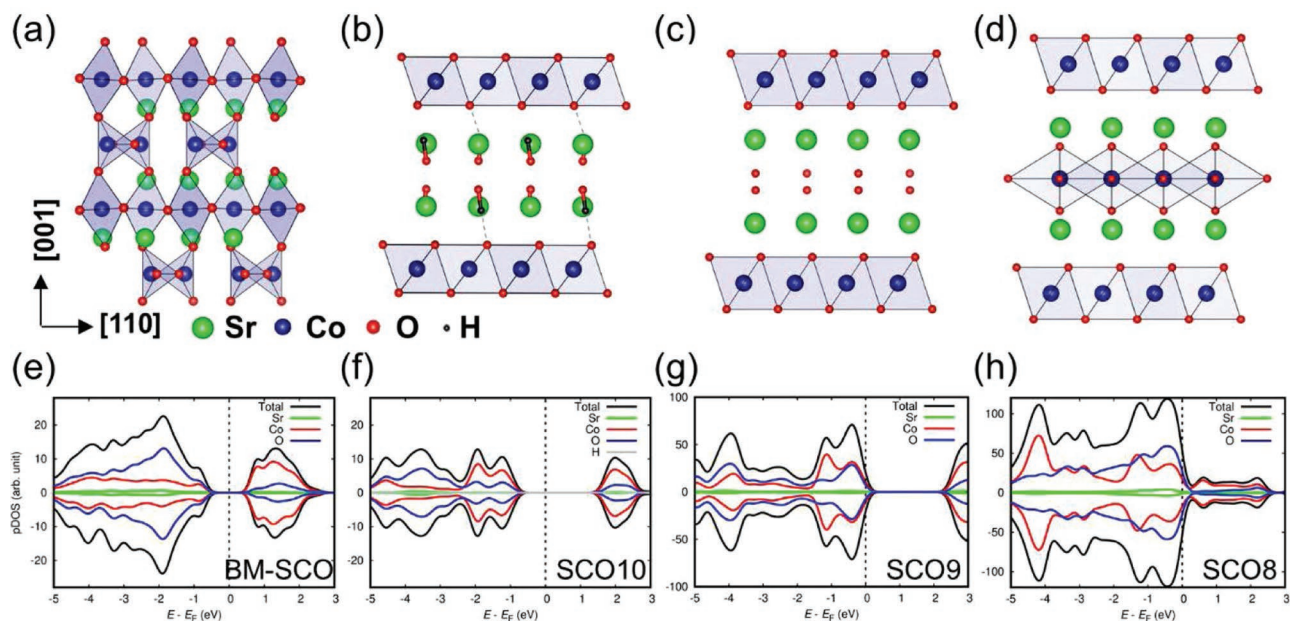


Figure 5. Atomic structures of a) BM-SCO, b) SCO10, c) SCO9, and d) SCO8 (110) plane. e–h) The corresponding pDOS as calculated with first-principles DFT methods.

thermoreflectance (TDTR) method. TDTR method has been subjected to characterize thermal properties of both bulk and thin film materials.^[21,44,45] The error bars in Figure 4f arise mainly from the physical parameter uncertainties, raw data spreads, and statistic standard deviations (see Experiment Section). It seems that higher oxygen deficiency leads to lower thermal conductivity in layered-SCOs. At room temperature, the κ of the four SCO9 lowers down to $0.33 \text{ W K}^{-1} \text{ m}^{-1}$, which is only 44% of that in BM-SCO and much lower than $\text{Na}_x\text{Co}_2\text{O}_4$.^[46] The model majority $\text{V}_\text{O}^\bullet$ in RS layer and minority $\text{V}_\text{O}^\bullet$ in CoO_2 layer again endorses the lowest thermal conductivity in SCO9 as it hosts the most sintered $\text{V}_\text{O}^\bullet$ in RS layer. The exceptional suppression of κ in SCO10 probably arises from the extra protons in the material.^[21] We did not give the figure of merit ZT because in thin film the thermal conductivity was probed along out-of-plane direction, while the PF was measured in in-plane direction. It is worth mentioning that although a direct measurement of in-plane κ is quite challenge for thin film, it could be estimated by notifying the thermal conductivity anisotropy. In highly crystalline samples of $\text{Ca}_3\text{Co}_4\text{O}_9$, the in-plane thermal conductivity is twice of that along out-of-plane.^[47] Since the crystal structure of SCO8 is very similar to $\text{Ca}_3\text{Co}_4\text{O}_9$, its in-plane κ could be roughly estimated as $1.26 \text{ W K}^{-1} \text{ m}^{-1}$. However, such estimation may not appropriate for SCO10 and SCO9 as they have different RS structures.

In the last decades, dozens of thermoelectric oxides like n-type perovskite $\text{CaMnO}_{3-\delta}$,^[48–50] $\text{SrTiO}_{3-\delta}$,^[51–54] $\text{Cd}_3\text{TeO}_{6-\delta}$,^[55] p-type $\text{Na}_x\text{CoO}_{2-\delta}$,^[39,56,57] $\text{Ca}_3\text{Co}_4\text{O}_{9,67-\delta}$,^[37,58,59] and $\text{Bi}_2\text{Sr}_2\text{Co}_2\text{O}_{8,4-\delta}$,^[60,61] have been synthesized. However, the oxygen deficiency was limited to a very small range ($\delta < 0.5$) even under extreme synthesis environments, especially as regards p-type layered compounds.^[60,62–64] The formation of the large oxygen deficiency in layered compounds remains a big challenge and the resulting effects on the accompanying performances have yet to

be explored. Here, we show that large oxygen deficiency could greatly improve the thermoelectric performance of layered oxides by forming sintered $\text{V}_\text{O}^\bullet$.

The above experiments reveal that $\text{V}_\text{O}^\bullet$ properly distributed in different layers significantly enhances the electric and thermoelectric performances of layered SCOs. It is also interesting to know how these SCOs behave without $\text{V}_\text{O}^\bullet$, thus we carried out density functional theory (DFT) based first-principles calculations for stoichiometric SCOs. Figure 5 shows the (110) atomic plane of BM-SCO, SCO10, SCO9, and SCO8 as well as their projected density of states (pDOS). The corresponding $(\bar{1}\bar{1}0)$ and (100) atomic planes are given in Figure S8, Supporting Information. The pDOS in Figure 5e–h clearly shows that in stoichiometric SCO9 and SCO8 the Fermi energy level shifts toward the valence band as compared to BM-SCO and SCO10, indicating a very high filling level of carriers. The SCO8 polymorph even switches to metallic as a result of the introduction of Co ions into the corresponding RS layers. The doping of oxygen vacancies into the material would trap the holes and result in the decrease of the carrier concentration. High carrier concentration is generally unwanted in thermoelectric materials as it typically leads to a suppression in the Seebeck coefficient. In SCO9 and SCO8 thin films, the incorporated $\text{V}_\text{O}^\bullet$ limits the theoretical high carrier concentration to the level of SCO10 (Figure S6, Supporting Information), thereby prevents a sharp decline in Seebeck coefficient. This calculation reveals that $\text{V}_\text{O}^\bullet$, including sintered $\text{V}_\text{O}^\bullet$ in RS layer, plays an essential role in maintaining the Seebeck coefficient in layered oxides.

3. Conclusion

In summary, three layered Sr–Co–O thin films (SCO10, SCO9, and SCO8) consisting of alternate stacking of RS nano-blocks

and CoO₂ frame layers, that is, [Sr₂O₂H₂]_{0.5}CoO₂, [Sr₂O₂]_{0.4}CoO₂, and [Sr₂CoO₃]_{0.57}CoO₂ were synthesized from parent brownmillerite SrCoO_{2.5} thin films step-by-step. It is found that the oxygen deficiency in layered SCOs could be greatly promoted to 0.84 in SCO8 and 2.95 in SCO9 from 0.08 in SCO10 by reconstructing the RS nano-blocks, while still demonstrating elevated electronic conductivity. The compound SCO9 with the highest δ (2.95) exhibited the best PF (3.6 mW K⁻² m⁻¹), output power density (4.5 W m⁻² at $\Delta T = 28$ K), and lowest κ (0.33 W K⁻¹ m⁻¹) at room temperature, which is on par with Bi₂Te₃ benchmark. Experiment results combining with theoretical calculations reveal that the enhanced electric and thermoelectric properties benefit from the V_o^{••} properly distributed in different layers, that is, a majority of sintered V_o^{••} in insulating rock-salt layer and a minority of normal V_o^{••} in conductive CoO₂ layer.

We offered a new route to synthesis layered oxides with variable nano-blocks from brownmillerites, and pointed out the importance of oxygen deficiency and its distribution in tailoring the physical and chemical properties of transition-metal oxides. The sintered/normal V_o^{••} superlattice model provides guidance to the exploration of materials with both low electric resistivity and thermoelectric conductivity. Further study on obtaining higher oxygen deficiency and whether the two types V_o^{••} are transferable across the RS and CoO₂ layer is highly desired.

4. Experimental Section

Sample Preparation: The BM-SCO thin films were deposited on (001) LSAT substrates by pulsed laser deposition. The growth conditions were a temperature of 750 °C, oxygen pressure of 13 Pa, laser energy density of 1.5 J cm⁻², and laser frequency of 6 Hz. The film thickness was ≈ 70 nm for 4000 pulses deposition. The SCO10 thin film was obtained by annealing BM-SCO in 10 bar CO₂ + H₂O at 450 °C for 1 h, and then in air at 400 °C for another 1 h. The SCO10 transformed to SCO9 by annealing sample in air at 550 °C for 3 h. The SCO8 was obtained by further annealing the SCO9 thin film in air at 700 °C for 1 h.

Structure and Properties: The sample structure was characterized by a high-resolution X-ray diffractometer (Rigaku SmartLab, 45 kV, 200 mA, $\lambda = 1.5406$ Å). The temperature dependent XRD was carried out with a domed stage (Anton Paar, DHS 1100). The heating rate was 30 °C min⁻¹. Each scan took ≈ 2 min. HAADF-STEM, EDS, and ABF were conducted using a double aberration-corrected transmission electron microscopy (Thermo Fisher Themis Z G2 60–300) operated at 300 kV. The EELS spectra were collected at a beam current of about 100 pA by a Gatan Quantum 965 spectrometer. The XAS was taken at beamline 4B9B of Beijing Synchrotron Radiation Facility in the total fluorescence yield mode. The electric resistivity was measured using a four-probe method by a Quantum Design PPMS. Prior to the measurement, 4 Pt square pads (500 $\mu\text{m} \times 500 \mu\text{m}$, 100 nm thick) with 1 mm space were deposited onto the SCO thin film by magneto-sputtering. These pads were aligned in a line geometry and parallel to one edge of the substrate. Then they were connected to the electric puck with Al wire by ultrasonic wire-bonding. The resistance was measured by collecting the current flowing through the four pads and the corresponding voltage across on the middle two pads. The resistivity of BM-SCO was measured by a Keithley 6517B picometer with a two-probe connection. The Hall conduction of the thin films was measured using a van der Pauw method, and an error margin within 2% was generated during the curve fitting (Hall resistance vs magnetic field) in obtaining the Hall coefficient. Thus, there were error margins of 2% for mobility and carrier concentration. The optical transmittance of these thin films was measured by a PerkinElmer LAMBDA 950 spectrometer using a two-side polished substrate. Prior to the measurement, the absorption was calibrated by

referring to a bare substrate. The Seebeck coefficient of the thin films was measured using a Quantum Design PPMS. The room temperature Seebeck coefficient was verified using a portable thermoelectric monitor (PTM-3, JouleYacht). The output power of layered-SCO thin films was measured by collecting the voltage and current of an external loading resistor while varying its resistance at a given temperature difference (ΔT). The inset in Figure 4g illustrates the schematic experiment setup for this measurement. The size of the sample was 10 mm \times 10 mm. The space between the two electrodes was 9 mm. The high temperature end (T_{high}) was heated by a hot-plate, while the low temperature end (T_{low}) was cooled by a copper plate at room temperature. The sample was stabilized for 15 min prior to the measurement. The ΔT between T_{high} and T_{low} was estimated by using V_{oc} (open circuit voltage) = ΔT , which was quite close to the value monitored by thermal couples, see Table S2, Supporting Information. It was noticed that the measured temperature difference was 2–3 K lower than that estimated from V_{oc}/S . To avoid any exaggeration, the latter was used to calculate the normalized output power density. The voltage and current of the loading resistor were measured by a Keithley 2400 nanovoltmeter and 2182 ampere meter, respectively.

TDTR: The out-of-plane thermal conductivity of these SCO thin films was measured by a TDTR method. Prior to the measurement, a ≈ 80 nm Al layer was coated onto the samples by magnetron sputtering as an optical transducer. The samples were mounted on an optical cryostat (Montana Instruments) and cooled using liquid helium for low-temperature measurements. TDTR is a transient method utilizing femtosecond laser pulses both as a heat source and sensor based on the pump–probe principle. Femtosecond laser pulses ($\lambda = 770$ nm) were generated by a Ti:sapphire laser (Chameleon, Coherent), and was then split using a polarization beam splitter into the pump beam that heated the sample and the probe beam that sensed the temperature decay. The pump beam was modulated using an electro-optic modulator (Conoptics 350) at 9.8 MHz. To increase the signal-to-noise ratio, the probe beam was modulated using a mechanical chopper at ≈ 175 Hz. The size of two beam spots was chosen to be $\approx 26 \mu\text{m}$ in diameter to guarantee 1D heat dissipation. As the reflectivity of Al layer changed linearly with temperature, the intensity of the reflected probe beam was very sensitive to the temperature variation. A delay time of 0–4000 ps between pump and probe pulses was obtained with a 600 mm delay stage. Prior to the signal detection, most of the pump laser was filtered using a two-tint method. The in-phase (V_{in}) and out-of-phase (V_{out}) signals varying with the delay time were collected using a Si photodetector and extracted with a lock-in amplifier (Zurich Instruments, HF2LI). The ratio $-V_{\text{in}}/V_{\text{out}}$ was finally fitted to a multi-layer thermal transport model to obtain the thermal conductivity. The error bars in Figure 4f arise mainly from the physical parameter uncertainties, raw data spreads, and statistic standard deviations. The first one was propagated from the uncertainties in film thickness ($\approx 3\%$), laser spot size ($\approx 10\%$), and specific heat of each layer ($\approx 5\%$). Figure S9, Supporting Information demonstrates a set of TDTR raw data, their fitted curves at optimum, and with 10% uncertainties at different temperature for these SCO thin films. It could be seen that nearly all data points fall into the 10% uncertainties range. Therefore, the error margin amounts to $\approx 10\%$ in total from these two aspects. The latter originated from the standard deviation of three individual measurements at different locations on sample surface. In most cases it was less than 10%, while at 350 K a large deviation (19% for BM-SCO, 39% for SCO10, and 21% for SCO8) was observed due to the temperature variation when heating the sample.

First-Principles Calculations: Spin-polarized DFT^[65] calculations were performed to theoretically characterize the structural, mechanical, and electronic properties of SCO polymorphs. The PBEsol functional^[66] was used as implemented in the VASP software.^[67] A “Hubbard- U ” scheme^[68] with $U = 4$ eV was employed for a better treatment of the localized Co 3d electronic orbitals.^[69] The “projector augmented wave” method was used to represent the ionic cores^[70] by considering the following electrons as valence: Sr 4s, 4p, and 5s; Co 3d and 4s; O 2s and 2p; H 1s. Wave functions were represented in a plane-wave basis truncated at 650 eV. For integrations within the first Brillouin zone, thick Monkhorst–Pack k -point

grids were employed with a density equivalent to that of $16 \times 16 \times 16$ for a conventional 5-atoms perovskite unit cell. Periodic boundary conditions were applied along the three lattice vectors of the simulation supercell. Geometry relaxations were performed with a conjugate-gradient algorithm that optimized the ionic positions and the volume and shape of the simulation cell. The relaxations were halted when the forces in the atoms were all below $0.005 \text{ eV } \text{Å}^{-1}$. By using these technical parameters, the obtained energies were converged to within 0.5 meV per formula unit. Different possible spin magnetic arrangements involving the electronic Co d orbitals (i.e., ferromagnetic and antiferromagnetic type A, C, and $G^{(7)}$) were explored in the DFT calculations. For the calculation of electronic densities of states, the more accurate range-separated hybrid functional HSE06 was employed.^[72]

Supporting Information

Supporting Information is available from the Wiley Online Library or from the author.

Acknowledgements

The authors acknowledge support by the National Natural Science Foundation of China (11804145, 51972160, and 12004156), the Science and Technology Research Items of Shenzhen (JCYJ20180504165650580, JCYJ20190809142603695, JCYJ20190809181601639), Guangdong Basic and Applied Basic Research Foundation 2019A1515110519. The authors would like to thank the Core Research Facilities, Southern University of Science and Technology and BSRF. C.C. acknowledges support from the Spanish Ministry of Science, Innovation, and Universities under the “Ramón y Cajal” fellowship RYC2018-024947-I.

Conflict of Interest

The authors declare no conflict of interest.

Data Availability Statement

The data that support the findings of this study are available from the corresponding author upon reasonable request.

Keywords

layered structures, oxygen vacancies, resistivity, thermoelectrics, thin films

Received: April 29, 2022

Revised: May 17, 2022

Published online:

- [1] C. Bi, Y. Liu, T. Newhouse-Illige, M. Xu, M. Rosales, J. W. Freeland, O. Mryasov, S. Zhang, S. G. E. te Velthuis, W. G. Wang, *Phys. Rev. Lett.* **2014**, *113*, 267202.
- [2] H.-B. Li, N. Lu, Q. Zhang, Y. Wang, D. Feng, T. Chen, S. Yang, Z. Duan, Z. Li, Y. Shi, W. Wang, W.-H. Wang, K. Jin, H. Liu, J. Ma, L. Gu, C. Nan, P. Yu, *Nat. Commun.* **2017**, *8*, 2156.
- [3] J. Jeong, N. Aetukuri, T. Graf, T. D. Schladt, M. G. Samant, S. S. P. Parkin, *Science* **2013**, *339*, 1402.
- [4] N. Lu, P. Zhang, Q. Zhang, R. Qiao, Q. He, H.-B. Li, Y. Wang, J. Guo, D. Zhang, Z. Duan, Z. Li, M. Wang, S. Yang, M. Yan, E. Arenholz, S. Zhou, W. Yang, L. Gu, C.-W. Nan, J. Wu, Y. Tokura, P. Yu, *Nature* **2017**, *546*, 124.
- [5] Z. Xiao, Y. Wang, Y.-C. Huang, Z. Wei, C.-L. Dong, J. Ma, S. Shen, Y. Li, S. Wang, *Energy Environ. Sci.* **2017**, *10*, 2563.
- [6] J. Kim, X. Yin, K. C. Tsao, S. Fang, H. Yang, *J. Am. Chem. Soc.* **2014**, *136*, 14646.
- [7] N. Mahato, A. Banerjee, A. Gupta, S. Omar, K. Balani, *Prog. Mater. Sci.* **2015**, *72*, 141.
- [8] B. Duan, Y. Li, J. Li, Y. Gao, P. Zhai, J. Yang, Z. Lu, H. Yang, H. Wang, G. Li, *Ceram. Int.* **2020**, *46*, 26176.
- [9] G.-K. Ren, J.-L. Lan, K. J. Ventura, X. Tan, Y.-H. Lin, C.-W. Nan, *npj Comput. Mater.* **2016**, *2*, 16023.
- [10] Y. Tsujimoto, C. Tassel, N. Hayashi, T. Watanabe, H. Kageyama, K. Yoshimura, M. Takano, M. Ceretti, C. Ritter, W. Paulus, *Nature* **2007**, *450*, 1062.
- [11] K. T. Kang, C. J. Roh, J. Lim, T. Min, J. H. Lee, K. Lee, T. Y. Lee, S. Kang, D. Seol, J. Kim, H. Ohta, A. Khare, S. Park, Y. Kim, S. C. Chae, Y. S. Oh, J. Lee, J. Yu, J. S. Lee, W. S. Choi, *Adv. Mater.* **2019**, *31*, 1808104.
- [12] H. Jeon, W. S. Choi, M. D. Biegalski, C. M. Folkman, I. C. Tung, D. D. Fong, J. W. Freeland, D. Shin, H. Ohta, M. F. Chisholm, H. N. Lee, *Nat. Mater.* **2013**, *12*, 1057.
- [13] H. B. Li, S. Kobayashi, C. Zhong, M. Namba, Y. Cao, D. Kato, Y. Kotani, Q. Lin, M. Wu, W. H. Wang, M. Kobayashi, K. Fujita, C. Tassel, T. Terashima, A. Kuwabara, Y. Kobayashi, H. Takatsu, H. Kageyama, *J. Am. Chem. Soc.* **2021**, *143*, 17517.
- [14] Q. Zhang, X. He, J. Shi, N. Lu, H. Li, Q. Yu, Z. Zhang, L. Q. Chen, B. Morris, Q. Xu, P. Yu, L. Gu, K. Jin, C. W. Nan, *Nat. Commun.* **2017**, *8*, 104.
- [15] D. Li, K. Lee, B. Y. Wang, M. Osada, S. Crossley, H. R. Lee, Y. Cui, Y. Hikita, H. Y. Hwang, *Nature* **2019**, *572*, 624.
- [16] S. Chen, H. Zhou, X. Ye, Z. Chen, J. Zhao, S. Das, C. Klewe, L. Zhang, E. Lupi, P. Shafer, E. Arenholz, D. Jin, H. Huang, Y. Lu, X. Li, M. Wu, S. Ke, H. Xu, X. Zeng, C. Huang, L. W. Martin, L. Chen, *Adv. Funct. Mater.* **2019**, *29*, 1907072.
- [17] L. Cao, O. Petravic, P. Zakalek, A. Weber, U. Rücker, J. Schubert, A. Koutsoubas, S. Mattauch, T. Brückel, *Adv. Mater.* **2019**, *31*, 1806183.
- [18] X. Guo, R. Waser, *Prog. Mater. Sci.* **2006**, *51*, 151.
- [19] H. Jeon, W. S. Choi, J. W. Freeland, H. Ohta, C. U. Jung, H. N. Lee, *Adv. Mater.* **2013**, *25*, 3651.
- [20] Q. Yang, J. Lee, B. Feng, Y. Ikuhara, G. Kim, H. J. Cho, H. Jeon, H. Ohta, *ACS Appl. Electron. Mater.* **2020**, *2*, 2250.
- [21] Q. Lu, S. Huberman, H. Zhang, Q. Song, J. Wang, G. Vardar, A. Hunt, I. Waluyo, G. Chen, B. Yildiz, *Nat. Mater.* **2020**, *19*, 655.
- [22] H.-B. Li, F. Lou, Y. Wang, Y. Zhang, Q. Zhang, D. Wu, Z. Li, M. Wang, T. Huang, Y. Lyu, J. Guo, T. Chen, Y. Wu, E. Arenholz, N. Lu, N. Wang, Q. He, L. Gu, J. Zhu, C.-W. Nan, X. Zhong, H. Xiang, P. Yu, *Adv. Sci.* **2019**, *6*, 1901432.
- [23] T. Katayama, A. Chikamatsu, H. Kamisaka, Y. Yokoyama, Y. Hirata, H. Wadati, T. Fukumura, T. Hasegawa, *AIP Adv.* **2015**, *5*, 107147.
- [24] S. Hu, Y. Zhu, W. Han, X. Li, Y. Ji, M. Ye, C. Jin, Q. Liu, S. Hu, J. Wang, J. Wang, J. He, C. Cazorla, L. Chen, *Adv. Mater.* **2021**, *33*, 2104623.
- [25] Y. Long, Y. Kaneko, S. Ishiwata, Y. Taguchi, Y. Tokura, *J. Phys.: Condens. Matter* **2011**, *23*, 245601.
- [26] S. Hu, W. Han, S. Hu, J. Seidel, J. Wang, R. Wu, J. Wang, J. Zhao, Z. Xu, M. Ye, L. Chen, *Chem. Mater.* **2019**, *31*, 6117.
- [27] T. Mizokawa, Y. Wakisaka, T. Sudayama, C. Iwai, K. Miyoshi, J. Takeuchi, H. Wadati, D. G. Hawthorn, T. Z. Regier, G. A. Sawatzky, *Phys. Rev. Lett.* **2013**, *111*, 056404.
- [28] D. K. Bora, X. Cheng, M. Kapilashrami, P. A. Glans, Y. Luo, J. H. Guo, *J. Synchrotron Radiat.* **2015**, *22*, 1450.
- [29] W. S. Yoon, M. Balasubramanian, K. Y. Chung, X. Q. Yang, J. McBreen, C. P. Grey, D. A. Fischer, *J. Am. Chem. Soc.* **2005**, *127*, 17479.

- [30] L. Gao, X. Chen, X. Lyu, G. Ji, Z. Chen, M. Zhu, X. Cao, C. Li, A. Ji, Z. Cao, N. Lu, *J. Phys.: Condens. Matter* **2021**, *33*, 104004.
- [31] Q. Y. Lu, Y. Chen, H. Bluhm, B. Yildiz, *J. Phys. Chem. C* **2016**, *120*, 24148.
- [32] S. Stemmer, A. Sane, N. D. Browning, T. J. Mazanec, *Solid State Ionics* **2000**, *130*, 71.
- [33] D. Pelloquin, S. Hébert, A. Maignan, B. Raveau, *Solid State Sci.* **2004**, *6*, 167.
- [34] A. Sakai, T. Kanno, S. Yotsuhashi, A. I. Odagawa, H. Adachi, in IEEE ICT 2005. 24th Int. Conf. Thermoelectrics, IEEE, Piscataway **2005**.
- [35] L. Malavasi, C. A. J. Fisher, M. S. Islam, *Chem. Soc. Rev.* **2010**, *39*, 4370.
- [36] J. Wang, B.-Y. Zhang, H.-J. Kang, Y. Li, X. Yaer, J.-F. Li, Q. Tan, S. Zhang, G.-H. Fan, C.-Y. Liu, L. Miao, D. Nan, T.-M. Wang, L.-D. Zhao, *Nano Energy* **2017**, *35*, 387.
- [37] B. Paul, E. M. Bjork, A. Kumar, J. Lu, P. Eklund, *ACS Appl. Energy Mater.* **2018**, *1*, 2261.
- [38] M. Ohtaki, T. Tsubota, K. Eguchi, H. Arai, *J. Appl. Phys.* **1996**, *79*, 1816.
- [39] I. Terasaki, Y. Sasago, K. Uchinokura, *Phys. Rev. B* **1997**, *56*, R12685.
- [40] H. You, Z. Li, Y. Shao, X. Yuan, W. Liu, H. Tang, Q. Zhang, Y. Yan, X. Tang, *Appl. Therm. Eng.* **2022**, *202*, 117818.
- [41] J. Liang, T. Wang, P. Qiu, S. Yang, C. Ming, H. Chen, Q. Song, K. Zhao, T.-R. Wei, D. Ren, Y.-Y. Sun, X. Shi, J. He, L. Chen, *Energy Environ. Sci.* **2019**, *12*, 2983.
- [42] Y. Lu, Y. Qiu, K. Cai, Y. Ding, M. Wang, C. Jiang, Q. Yao, C. Huang, L. Chen, J. He, *Energy Environ. Sci.* **2020**, *13*, 1240.
- [43] B. Lee, H. Cho, K. T. Park, J. S. Kim, M. Park, H. Kim, Y. Hong, S. Chung, *Nat. Commun.* **2020**, *11*, 5948.
- [44] C. Di, J.-H. Pan, S.-T. Dong, Y.-Y. Lv, X.-J. Yan, J. Zhou, S.-H. Yao, H. Lu, V. E. Gusev, Y.-F. Chen, M.-H. Lu, *CrystEngComm* **2019**, *21*, 6261.
- [45] X.-J. Yan, Y.-Y. Lv, L. Li, X. Li, S.-H. Yao, Y.-B. Chen, X.-P. Liu, H. Lu, M.-H. Lu, Y.-F. Chen, *Appl. Phys. Lett.* **2017**, *110*, 211904.
- [46] K. Takahata, Y. Iguchi, D. Tanaka, T. Itoh, I. Terasaki, *Phys. Rev. B* **2000**, *61*, 12551.
- [47] B. Paul, Y. Zhang, W. Zhu, B. Xin, G. Ramanath, T. Borca-Tasciuc, P. Eklund, *Appl. Phys. Lett.* **2022**, *120*, 061904.
- [48] E. Bakken, T. Norby, S. Stolen, *Solid State Ionics* **2005**, *176*, 217.
- [49] M. Molinari, D. A. Tompsett, S. C. Parker, F. Azough, R. Freer, *J. Mater. Chem. A* **2014**, *2*, 14109.
- [50] R. U. Chandrasena, W. Yang, Q. Lei, M. U. Delgado-Jaime, K. D. Wijesekara, M. Golalikhani, B. A. Davidson, E. Arenholz, K. Kobayashi, M. Kobata, F. M. F. de Groot, U. Aschauer, N. A. Spaldin, X. Xi, A. X. Gray, *Nano Lett.* **2017**, *17*, 794.
- [51] X.-L. Shi, H. Wu, Q. Liu, W. Zhou, S. Lu, Z. Shao, M. Dargusch, Z.-G. Chen, *Nano Energy* **2020**, *78*, 105195.
- [52] C. Yu, M. L. Scullin, M. Huijben, R. Ramesh, A. Majumdar, *Appl. Phys. Lett.* **2008**, *92*, 191911.
- [53] S. Lee, G. Yang, R. H. T. Wilke, S. Trolrier-McKinstry, C. A. Randall, *Phys. Rev. B* **2009**, *79*, 134110.
- [54] J. Liu, C. L. Wang, W. B. Su, H. C. Wang, P. Zheng, J. C. Li, J. L. Zhang, L. M. Mei, *Appl. Phys. Lett.* **2009**, *95*, 162110.
- [55] Y. J. Shan, K. Sasaki, K. Sudo, H. Imoto, M. Itoh, *Jpn. J. Appl. Phys., Part 2* **2002**, *41*, L780.
- [56] J. Xin, A. Basit, S. Li, S. Danto, S. C. Tjin, L. Wei, *Sensors* **2021**, *21*, 3437.
- [57] J. He, Y. Liu, R. Funahashi, *J. Mater. Res.* **2011**, *26*, 1762.
- [58] S. W. Li, R. Funahashi, I. Matsubara, K. Ueno, H. Yamada, *J. Mater. Chem.* **1999**, *9*, 1659.
- [59] X. Zhu, D. Shi, S. Dou, Y. Sun, Q. Li, L. Wang, W. Li, W. Yeoh, R. Zheng, Z. Chen, C. Kong, *Acta Mater.* **2010**, *58*, 4281.
- [60] Y. Morita, J. Poulsen, K. Sakai, T. Motohashi, T. Fujii, I. Terasaki, H. Yamauchi, M. Karppinen, *J. Solid State Chem.* **2004**, *177*, 3149.
- [61] H. Leligny, D. Grebille, O. Perez, A. C. Masset, M. Hervieu, B. Raveau, *Acta Crystallogr., Sect. B: Struct. Sci.* **2000**, *56*, 173.
- [62] M. Karppinen, H. Fjellvag, T. Konno, Y. Morita, T. Motohashi, H. Yamauchi, *Chem. Mater.* **2004**, *16*, 2790.
- [63] H. Yamauchi, K. Sakai, T. Nagai, Y. Matsui, M. Karppinen, *Chem. Mater.* **2006**, *18*, 155.
- [64] S. Ishiwata, I. Terasaki, Y. Kusano, M. Takano, *Phys. C* **2007**, *460*, 491.
- [65] C. Cazorla, J. Boronat, *Rev. Mod. Phys.* **2017**, *89*, 035003.
- [66] J. P. Perdew, A. Ruzsinszky, G. I. Csonka, O. A. Vydrov, G. E. Scuseria, L. A. Constantin, X. Zhou, K. Burke, *Phys. Rev. Lett.* **2008**, *100*, 136406.
- [67] G. Kresse, J. Furthmüller, *Phys. Rev. B* **1996**, *54*, 11169.
- [68] S. L. Dudarev, G. A. Botton, S. Y. Savrasov, C. J. Humphreys, A. P. Sutton, *Phys. Rev. B* **1998**, *57*, 1505.
- [69] P. Rivero, C. Cazorla, *Phys. Chem. Chem. Phys.* **2016**, *18*, 30686.
- [70] P. E. Blochl, *Phys. Rev. B* **1994**, *50*, 17953.
- [71] C. Cazorla, O. Dieguez, J. Iniguez, *Sci. Adv.* **2017**, *3*, e1700288.
- [72] J. Heyd, G. E. Scuseria, M. Ernzerhof, *J. Chem. Phys.* **2003**, *118*, 8207.